

Influence of processing conditions on strut structure and compressive properties of cellular lattice structures fabricated by selective laser melting

Chunlei Qiu^{a,*}, Sheng Yue^{b,c}, Nicholas J.E. Adkins^a, Mark Ward^a, Hany Hassanin^a, Peter D. Lee^{b,c}, Philip J. Withers^{b,c}, Moataz M. Attallah^a

^a School of Metallurgy and Materials, University of Birmingham, Edgbaston, Birmingham B15 2TT, UK

^b School of Materials, University of Manchester, Manchester M13 9PL, UK

^c Research Complex at Harwell, Rutherford Appleton Laboratory, Didcot, Oxfordshire OX11 0FA, UK

ARTICLE INFO

Article history:

Received 5 December 2014

Accepted 13 January 2015

Available online 30 January 2015

Keywords:

Additive manufacturing

Selective laser melting

Aluminium

Cellular lattice structures

Compression behaviour

3D quantification

ABSTRACT

AlSi10Mg cellular lattice structures have been fabricated by selective laser melting (SLM) using a range of laser scanning speeds and powers. The as-fabricated strut size, morphology and internal porosity were investigated using optical microscopy (OM), scanning electron microscopy (SEM) and X-ray microtomography (micro-CT) and correlated to the compressive properties of the structure. Strut diameter was found to increase monotonically with laser power while the porosity was largest at intermediate powers. Laser scanning speed was found to thicken the struts only at slow rates while the porosity was largest at intermediate speeds. High speed imaging showed the melt pool to be larger at high laser powers. Further the melt pool shape was found to vary cyclically over time, steadily growing before becoming increasingly instable and irregularly shaped before abruptly falling in size due to splashing of molten materials and the process repeating. Upon compressive loading, lattice deformation was homogeneous prior to the peak stress before falling sharply due to the creation of a (one strut wide) shear band at around 45° to the compression axis. The specific yield strength expressed as the yield stress/(yield stress of the aluminium × relative density) is not independent of processing conditions, suggesting that further improvements in properties can be achieved by process optimisation. Lattice struts failed near nodes by a mixture of ductile and brittle fracture.

© 2015 Elsevier B.V. All rights reserved.

1. Introduction

Cellular lattice structures have a wide range of applications, such as thermal insulation, shock or vibration damping, acoustic absorption, current collectors in battery electrodes, catalyst supports and biomedical implants [1–7]. Additive manufacturing technologies, such as selective laser melting and electron beam melting, have been widely used to fabricate cellular lattice structures [6–14] because of their capacity to fabricate fine (down to the micron level) complex freeform geometries directly from computer-aided design (CAD) models. To date there has been a focus on the optimisation of the lattice geometries (unit cell geometries, cell sizes and strut diameters) via CAD design [8–14]. However, the influence of processing conditions such as laser power and laser scanning speed on strut morphology and lattice performance is not so well understood. Yan

et al. [10] found the strut size of SLM-manufactured lattice structures to be slightly higher than those of the CAD designs, leading to denser parts, but to the best of the authors' knowledge to date a systematic study on the influence of processing condition on strut microstructure and hence properties is lacking, which is the aim of this paper.

In general, most of the studies on the deformation and failure mechanisms of lattice structures have been based on macroscopic observations rather than relating failure to strut integrity. The mechanical properties of various lattice architectures have been evaluated extensively, either experimentally by compression testing, or by finite element analysis [8–17]. Several authors have studied the deformation and fracture mechanisms of lattice structures [11–14]. Gümrük et al. [11,12] and McKown et al. [13] assessed the macroscopic shape change at different compressive strains and identified the development of shear bands during the deformation. Gorny et al. [14] demonstrated via SEM observation and the calculation of Tresca-strains that the failure of lattice structures was due to local strain concentrations.

While the testing of whole lattice structures has been extensive, systematic studies on the influence of processing conditions

* Corresponding author. Tel.: +44 121 414 7842; fax: +44 121 414 7890.

E-mail addresses: c.qiu@bham.ac.uk (C. Qiu), peter.lee@manchester.ac.uk (P.D. Lee), p.j.withers@manchester.ac.uk (P.J. Withers), m.m.attallah@bham.ac.uk (M.M. Attallah).

on the integrity of the individual struts are lacking. There is still disagreement over the mechanism by which porosity forms (especially spherical pores) in SLM-fabricated samples, although it is generally believed that irregular-shaped pores are caused by lack of fusion/melting [18–20]. Thijs et al. [21] attributed the formation of spherical pores to the collapse of key holes in an aluminium alloy but suggested that in a Ti-based alloy, spherical pores [22] were formed by powder denudation around the melt pool within a layer and an accumulation of the surface roughness across the layers. Vilaro et al. [23] suggested that the spherical pores were due to gas entrapment during melting and rapid solidification. Qiu et al. [24] directly observed open pores on the top surfaces of samples and argued that the spherical pores could be due to incomplete re-melting of some localised sites on the previous layer and to the insufficient feeding of molten metal to these sites.

The lack of clarity over the formation mechanism for spherical pores together with a poor understanding on the surface roughness development associated with SLM process [24] highlights the need for a better understanding on some of the fundamental phenomena associated with the SLM process, including the interaction between the laser beam and the molten pool.

In this paper, a parametric study has been performed to investigate the influence of processing conditions, such as laser power and scanning speed on lattice strut size, morphology, surface structure and internal porosity. High speed imaging has been applied to gain a better understanding of the evolution of the molten pool during laser scanning and the origin for the formation of pores and for the lattice structural development under different processing conditions. Alongside this, compression tests have been performed to correlate lattice structure performance with the SLM conditions.

2. Experimental

2.1. Lattice fabrication by SLM

Gas atomised AlSi10Mg (also called CL31) powder supplied by TLS Technik GmbH in the size range of 25–50 μm was used. A Concept Laser M2 Cusing SLM system which employs an Nd: YAG laser with a wavelength of 1075 nm and a constant beam spot size of 50 μm in diameter and a maximum laser output power of 400 W and a maximum laser scanning speed of 7000 mm/s has been used to prepare cellular lattice structures for characterisation and testing. The cellular lattice structures comprise nodally connected diamond unit cells (Fig. 1a and b). The strut diameter (D) and length (L) were designed to be 0.3 mm and 2 mm, respectively and the complete lattice structure has a dimension of $20 \times 20 \times 11 \text{ mm}^3$. To study the influence of processing conditions, such as laser power and laser scanning speed on lattice structures,

a set of structures were built at a constant laser scanning speed of 7000 mm/s but with laser powers ranging from 150 W to 400 W while another set of samples were built at a constant laser power of 400 W but with laser scanning speeds ranging from 1000 mm/s up to 7000 mm/s.

2.2. Microstructural characterisation and imaging

A JEOL 7000 FEG-SEM microscope has been used to study the as-fabricated lattice structures and struts. Prior to characterisation, all the lattice structures were ultrasonically cleaned in acetone for at least three minutes to remove any trapped loose powder or dirt. Several struts were snapped out of each lattice structure and examined by SEM. To measure the strut diameters from SEM micrographs, two parallel lines were drawn along the edges of a strut and the spacing between them determined (see Fig. 2b). Some lattice structures were mounted and then ground and polished for examination under an optical microscope to study the porosity distribution within the struts using tessellated micrographs to study large areas. The porosity was also quantified by 2D image analysis using ImageJ.

Some of the samples were imaged using a laboratory micro-CT system (Nikon X-Tek 225, Tring, United Kingdom) using an accelerating voltage of 80 kV and a filament current of 100 μA . The voxel size of the reconstructed volumes was 7.85 μm . The 3D volumes were then processed following the procedure of Yue et al. [25–26] so that porosity (both bulk and internal) and strut size distribution could be quantified. The strut diameter is expressed as that of the largest sphere that can be inscribed in the struts.

High speed imaging was also conducted using a Photron FASTCAM Mini UX100 high speed camera to better understand the influence of laser processing conditions on the molten pool. To observe the molten pools, the contrast was adjusted so that only very bright regions associated with high temperature melting or heating could be seen. The images were taken at a rate of 5000 frames/s.

2.3. Mechanical testing

Compression tests were performed at room temperature using a computer-controlled electric screw driven Zwick/Roell testing machine on as-fabricated lattice structures. Specimens with dimensions of $10 \times 10 \times 10 \text{ mm}^3$ were tested along their build direction (Z direction, as indicated in Fig. 1b). All the tests were conducted under displacement control at a rate of 0.2 mm/min. Some tests were also interrupted at different stages of compression and the specimens examined by SEM to study the deformation and fracture mechanisms of the lattice structures. The compression strengths are expressed in several different ways, including the nominal engineering strength (the maximum load

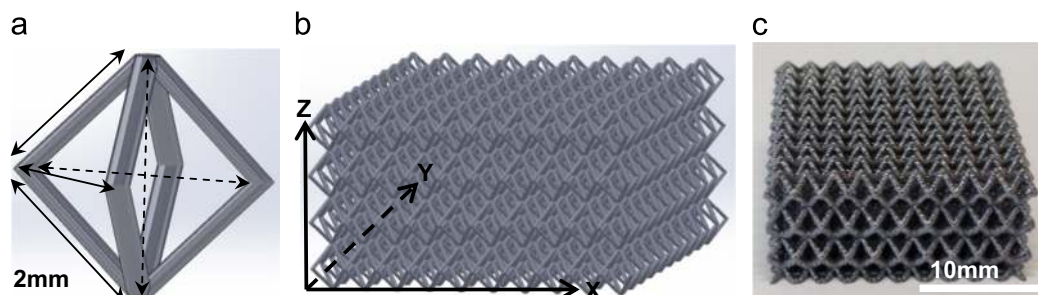


Fig. 1. (a) CAD model of the diamond unit cell; solid arrows show the 2 mm edges and struts and the dashed line arrows the 2.83 mm diagonals. (b) CAD model of lattice structure having a dimension of $20 \times 20 \times 11 \text{ mm}^3$ for SLM building (Z is build direction), and (c) an as-fabricated lattice structure.

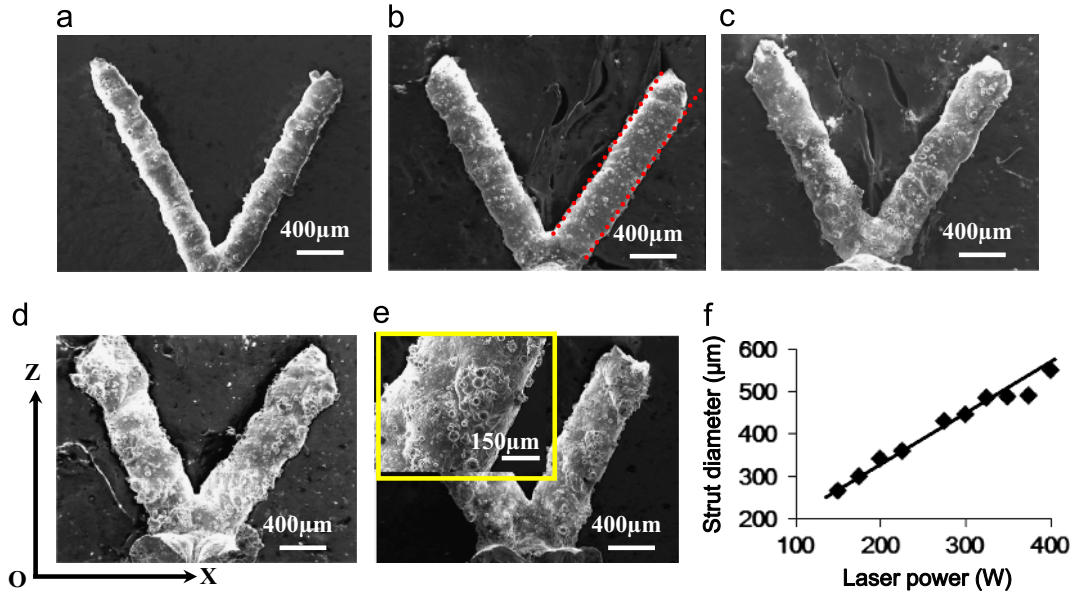


Fig. 2. (a–e) Secondary electron SEM images showing the variation of typical strut diameter and morphology with laser power: (a) 150 W; (b) 200 W; (c) 275 W; (d) 300 W; and (e) 375 W (scan speed 7000 mm/s). The inset in (e) shows a magnified view of the strut surface, (f) dependence of actual strut diameter on laser power (specified strut diameter 300 μm).

divided by the cross sectional area of the lattice structure) reflecting the load bearing capacity of the structure and the effective metal strength (the maximum load divided by the cross sectional area occupied by the struts (A) which is given by [27]).

$$A = n\pi R^2 / \sin \theta$$

where n is the number of lattice struts in a cross section of the lattice specimen which is 84 in the current study, R is the strut radius (measured by SEM) and θ is the strut inclination angle relative to the X – Y plane which is 45° in the current case.

The strengths are also expressed in normalised form, including normalised nominal yield strength ($\bar{\sigma}_o/\sigma_o$) which is the nominal yield strength of the lattice structures (1% offset plastic stress, $\bar{\sigma}_o$) divided by the yield strength of the parent alloy (σ_o which is around 250 MPa) and the specific normalised nominal yield strength ($\bar{\sigma}_o/\sigma_o\bar{\rho}$) which is defined as the normalised nominal yield strength divided by the relative density $\bar{\rho}$ of the lattice given by [27].

$$\bar{\rho} = \left(\frac{D}{L}\right)^2 \frac{\pi}{2 \sin \theta \cos^2 \theta} \left[1 - \left(\frac{D}{L}\right) \frac{(1 - \frac{1}{\pi} \sin^{-1}(\alpha))}{2\alpha \sin \theta \cos \theta} \right]$$

where D is the strut diameter (as measured by SEM), L is the strut length which is 2 mm, θ is the strut inclination angle relative to the X – Y plane which is 45° in the current case and $\alpha = 1/\sqrt{1 + \sin^2 \theta}$.

The strain was expressed in terms of nominal strain of the structure.

3. Results

3.1. Effect of laser power on lattice strut size and internal porosity

Fig. 2a–e shows struts taken from lattice structures fabricated using different laser powers at a fixed laser scanning speed (7000 mm/s). These clearly show that higher laser powers lead to much thicker struts with a nearly linear relationship (Fig. 2f). Consequently, the actual strut diameters deviate significantly from the specified diameter (namely 300 μm) by -40 μm (at 150 W) to $+200$ μm (at 400 W). This kind of deviation could be significant

when precise dimensions and shapes are required for a particular application. Moreover, it is noted that with increasing power an increasing number of partially melted powder particles adhered to the strut surfaces (see the inset in Fig. 2e).

Fig. 3 shows the variation in internal porosity within the struts as a function of laser power at a fixed laser scanning speed (7000 mm/s) as determined from OM images. It can be seen that at 150 W, the struts are generally dense, containing only a few pores. At 200 W and above, a few pores were present in all struts leading to a much higher porosity level. The contained porosity levels were found to drop at higher laser power levels. The pores were found to be spherical and free of unmelted powder particles, suggesting that their formation was not due to incomplete melting of powder or incomplete remelting of previous layers which usually leads to irregular-shaped or flat pores [18–20].

3.2. Effect of laser scanning speed on lattice strut size, morphology and internal porosity

Fig. 4 shows lattice structures fabricated at 400 W but at different laser scanning speeds. In contrast to the effect of varying the laser power, the laser scanning speed does not appear to affect strut diameter significantly for laser scanning speeds in the range of 3000–7000 mm/s. Consistent with Fig. 2, all the diameters recorded are greater than the target diameter (300 μm). Lattice struts fabricated at 3000 mm/s and 4000 mm/s tend to show more irregular shapes as shown in the inset.

Fig. 5 shows the porosity distribution in the lattice structures fabricated at different laser scanning speeds. It can be seen that struts fabricated with intermediate laser scanning speeds (3000–5000 mm/s) tend to have the greatest porosity ($\sim 2.8\%$).

Several samples were also analysed by micro-CT and the results are shown in Fig. 6 and Table 1. The 3D images are consistent with the 2D polished sections with the samples fabricated under 400 W–7000 mm/s and 400 W–1000 mm/s containing far more porosity than that fabricated at 150 W–7000 mm/s. While the changes in strut diameters with laser power and traverse speed are consistent too, the micro-CT measurements are around 30% smaller than those from 2D SEM observation because they were defined in 3D as the largest inscribed spheres in the struts. Also, the volume fraction of

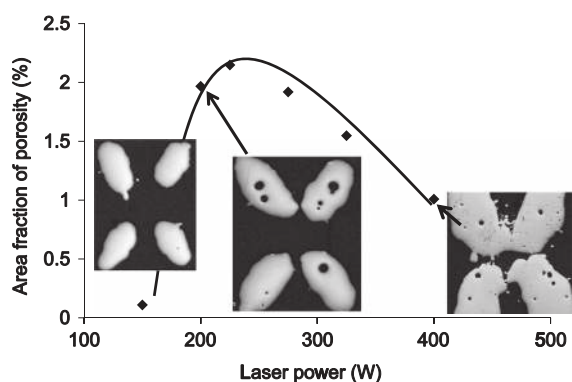


Fig. 3. Variation of porosity within the struts as a function of laser power at a traverse speed of 7000 mm/s along with the OM X–Z sectional images for 150 W, 200 W and 400 W laser powers. Micron markers represent 200 μm in each case.

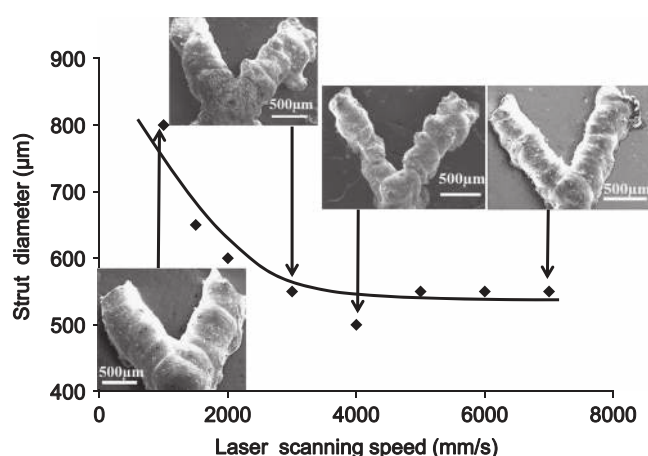


Fig. 4. Variation in strut diameter with laser scanning speed for lattices produced at 400 W along with SEM micrographs for 1000, 3000, 4000 and 7000 mm/s (specified strut diameter 300 μm).

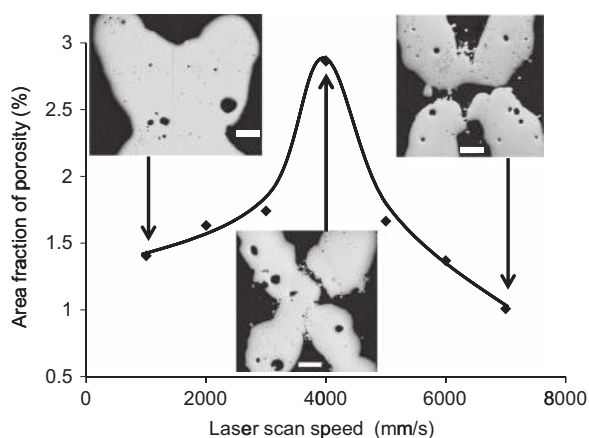


Fig. 5. Variation of porosity level in lattice structures fabricated at 400 W as a function of laser scanning speeds. The inset images are OM X–Z sections. Micron markers represent 200 μm in each case.

internal porosity is lower than the area fraction obtained by ImageJ to varied extents. The difference could be because the resolution (or the voxel size) of the micro-CT is 7.85 μm and the quantitative analysis does not include the finest pores.

Fig. 7 shows the microstructure of struts fabricated as a function of processing condition. It can be seen that the as-fabricated

microstructure is generally characterised by an $\alpha\text{-Al}$ matrix decorated with a Si network. The sample fabricated at 150 W–7000 mm/s, however, tends to show larger grains and coarser Si network than those fabricated at 400 W–7000 mm/s and 400 W–1000 mm/s.

3.3. High speed imaging of the melt pool

To understand the variation of size and morphology of the struts with processing conditions, high speed digital imaging has been carried out in a simple linear laser scanning mode under several different processing conditions. Videos 1, 2, and 3 show the results for SLM under 400 W–7000 mm/s, 400 W–1000 mm/s and 150 W–7000 mm/s, respectively. It is evident from these and Fig. 8 that the molten pool widths for 400 W–7000 mm/s and 400 W–1000 mm/s are much larger than that for 150 W–7000 mm/s. This would account for the above observation that the strut size increases with increased laser power. The interaction between the laser beam and the melt pool was also found to vary with processing conditions. At 400 W–7000 mm/s and 400 W–1000 mm/s, it appears to be very violent, characterised by considerable splashing of molten material out of the melt pool. This is most pronounced for the latter condition, causing knockout of large droplets out of the melt pool, suggesting that under this condition it may have been more turbulent. A more turbulent molten pool might also lead to wider spreading of molten material during cooling. This may account for the significant oversizing of struts under this condition (see Fig. 4).

Supplementary material related to this article can be found online at <http://dx.doi.org/10.1016/j.msea.2015.01.031>.

It is noteworthy that the molten pool size was not constant during laser melting. Instead, in each case, melting started with the development of a small/narrow molten pool followed by coarsening along with increased morphological irregularity, suggesting that the molten pool became increasingly unstable. This eventually led to splitting and splashing of material out of the melt pool. With the loss of material the molten pool reduced in size but it quickly built up again, repeating the above process.

3.4. Influence of processing conditions on mechanical properties

Fig. 9a shows a typical compression nominal engineering stress–strain curve. Initially the stress rises to a peak representing the maximum load-bearing capacity (Stage I). This is then followed by a drop and by a series of smaller peaks as the displacement increases. In Stage I the samples deformed uniformly without obvious fracture or collapse of lattice struts (see Fig. 9c). During Stage II, however, a shear band is developed at an angle of around 45° to the testing axis (see Fig. 9d). Within this shear band struts deform and rotate around their nodes towards the horizontal while the neighbouring struts experienced much less deformation. SEM examination (see Fig. 10) suggests that the lattice struts in the band have been partially fractured at the nodes, while the nodes and the surrounding struts remain fairly intact. During Stage III, the struts in the shear band have failed near the nodes, which leads to fragmentation of the lattice structure into two parts (see Fig. 9e). Stage IV is characterised by further disintegration of the structure into multiple parts, as shown in Fig. 9f. Evidently since the functionality of the structure is lost at the end of Stage I the behaviour in this stage is of primary interest from a load bearing viewpoint.

With regard to the effect of scan speed (Fig. 11b), it can be seen that the samples fabricated at 400 W–1000 mm/s, which have a strut diameter of 800 μm , show an extremely high load-bearing capacity (up to 36 MPa), much higher than the rest of the samples. The minimum in the load-bearing capacity vs scan speed curve is observed around 3000–4000 mm/s despite having similar strut

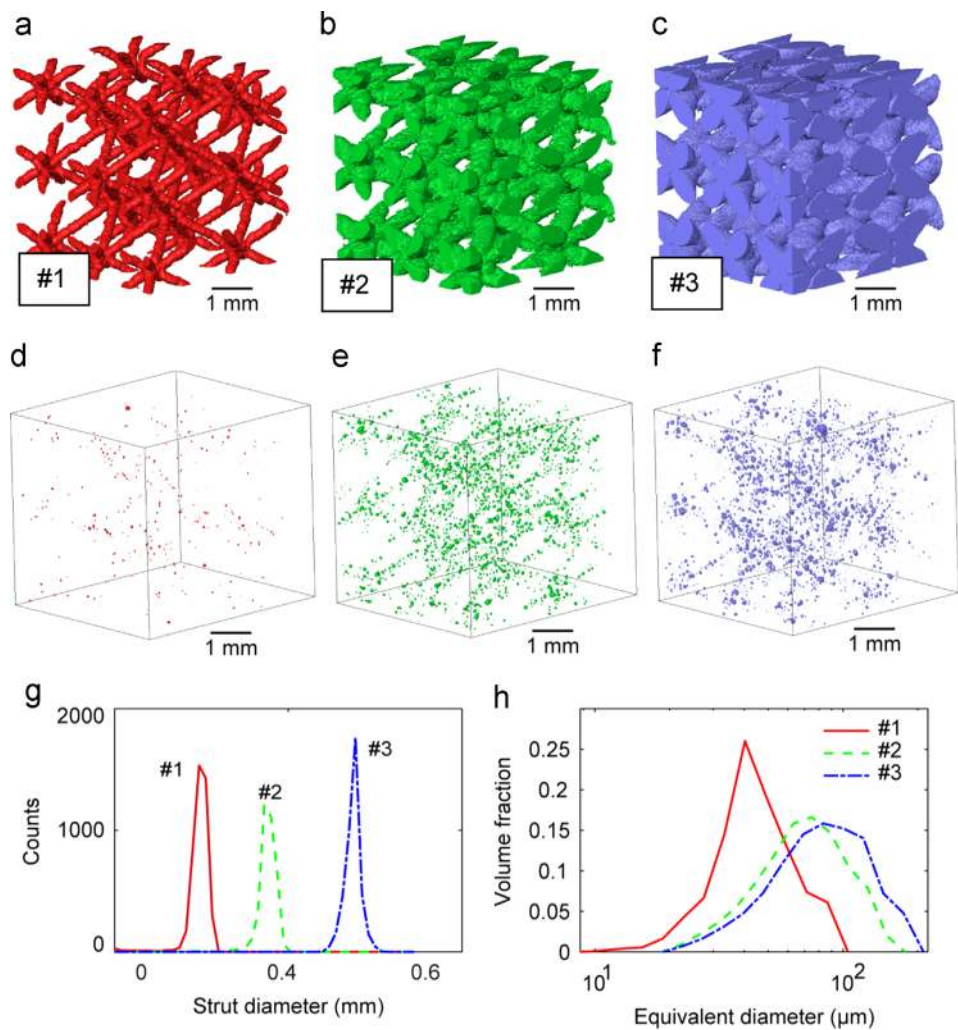


Fig. 6. (a–c) 3D rendering of the micro-CT volumes of samples and (d–f) the segmented pores for lattices built with (a) 150 W–7000 mm/s, (b) 400 W–7000 mm/s, and (c) 400 W–1000 mm/s. (g) Strut diameter distribution for three samples where #1, #2, #3 correspond to the processing conditions (a), (b) and (c), respectively. (h) Internal pore size distribution of the three samples.

Table 1
Quantitative analysis results on lattice struts and porosity for several samples.

Sample processing condition	Relative density (RD) (%)	Porosity fraction (only internal pores) (%)	Pore size mode (μm)	Modal strut diameter (μm)
150 W–7000 mm/s	6.2	0.08	40.3	210
400 W–7000 mm/s	18	0.70	74.8	360
400 W–1000 mm/s	5	0.38	83.2	555

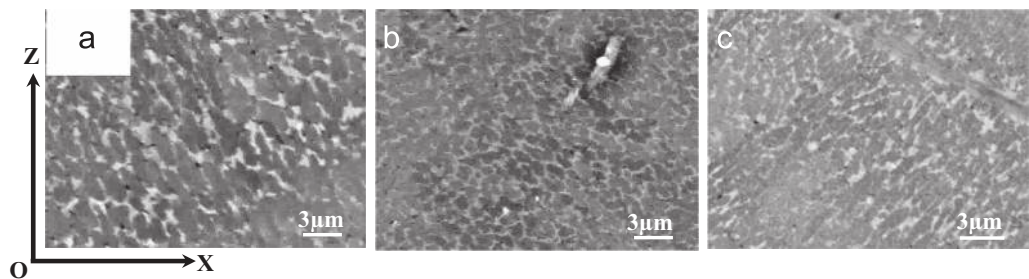


Fig. 7. Back scattered electron SEM images (X–Z sections) showing the microstructure of lattice struts fabricated at (a) 150 W–7000 mm/s; (b) 400 W–7000 mm/s; and (c) 400 W–1000 mm/s.

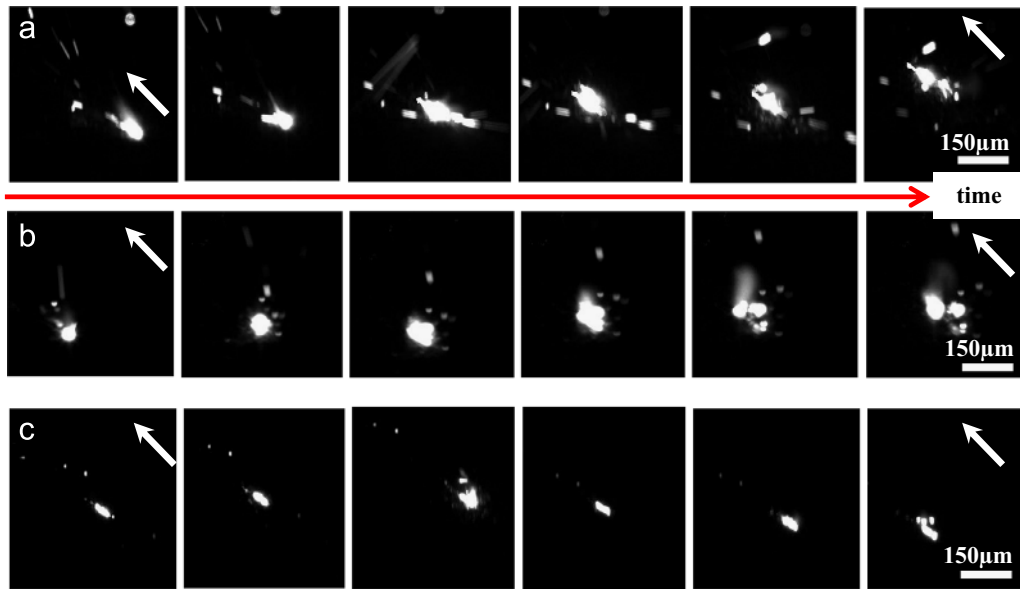


Fig. 8. Successive high speed imaging frames (0.2 millisecond apart) showing the melt pool development for (a) 400 W–7000 mm/s; (b) 400 W–1000 mm/s; and (c) 150 W–7000 mm/s. The white arrows show the direction of the laser beam. The scale bar is an approximate value but all the pictures were taken under the same camera set-up and magnification.

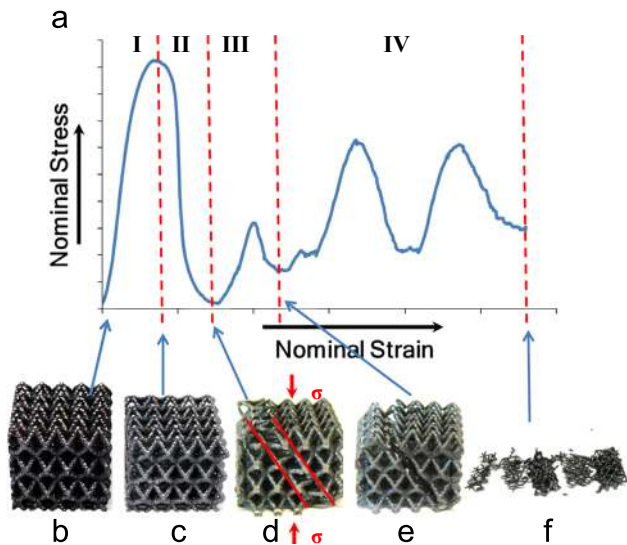


Fig. 9. (a) A typical compression stress–strain curve for as-manufactured samples (350 W–7000 mm/s) and lattice structure (b) before testing; and at the end of (c) Stage I, (d) Stage II, (e) Stage III and (f) Stage IV. The arrows and lines in Fig. 10 (d) show the loading direction and the shear band developed, respectively.

diameters to those of samples fabricated at 6000 mm/s and 7000 mm/s. This may be due to their increased irregularity in strut morphology/porosity as described above.

Unsurprisingly, the load-bearing capacity of the samples tested in this study generally increases with strut diameter (see Fig. 11c and Table 2).

It can be seen in Fig. 11d that the normalised nominal yield strength ($\bar{\sigma}_0/\sigma_0$) increases continuously with relative density, which is consistent with previous work [27–29]. However, relative density does not seem to be the only factor influencing the compression strengths given that the effective normalised nominal yield strength ($\bar{\sigma}_0/\sigma_0\bar{\rho}$) in Fig. 11e and f is not independent of processing conditions. Instead, it increases monotonically with laser power and varies with varied laser scanning speeds.

Similarly, the effective metal strength (maximum load/area of struts, Fig. 11e and f) was found to vary with laser power and scanning speed in a similar way. These results suggest that factors such as strut microstructure and structural integrity have an influence on the compressive properties of as-fabricated lattice structures.

Fig. 12 shows the typical fracture surfaces of the struts after compression testing. It can be seen that the fracture surfaces show a range of fracture micromechanisms from ductile dimpling suggestive of localised ductile failure, to lamellar fracture features (Fig. 12a–c). There are also some strut fracture surfaces where fine dimples prevail together with some pores that have opened-up (Fig. 12d–f). The cracking for this type of fracture is suspected to initiate at the sites of such pores, which then propagated outwards, leading to a ductile fracture.

4. Discussion

The current results clearly demonstrate that the strut diameter is affected by the laser power and scanning speed. This means that to fabricate a lattice structure with precisely dimensioned features for a particular application it is important to select the appropriate processing conditions or to account for the oversizing of the struts relative to the design diameter. The strut diameter was found to increase continuously with increased laser power at a constant scanning speed whereas strut diameter was affected by the scanning speed only at the lower end of scanning speeds. Unsurprisingly, high speed imaging revealed that laser beams of higher power lead to much wider melt pools than at lower power which when combined with low traverse speeds give rise to turbulent melt pool behaviour, spatter and pulsing of the pool size. These melt pool effects lead to a wider laser scanning track and thus to increased strut diameter as well as strut irregularity. That the melt pool width and strut diameter increase with laser power and decreased scanning speed is consistent with considerable previous work on welding [30–33] which suggests that the weld bead width increases with increased power and decreased traverse speed.

From the high speed imaging results, it can also be seen that the interaction between the laser beam and molten pool was particularly violent (characterised by splashing of molten material out of the molten pool) for processing conditions of 400 W–7000 mm/s and 400 W–1000 mm/s whereas it was much more stable for the condition of 150 W–7000 mm/s. The splashing is more likely to cause open pores and indents on the top layers [24]. This kind of defect could become entrained in the build given that successive layers followed the same violent scanning pattern. Also, the splashing would cause increased surface roughness on the top layers. With rough surfaces, the powder transfer to the previous layer would be heterogeneous, which is more likely to lead to development of defects such as pores. This is consistent with Thijs et al.'s work [22] which suggested that denudation of powder around the melt pool within a layer and an accumulation of the surface roughness across the layers could lead to formation of spherical pores. From the high speed imaging, no obvious keyhole mode welding could be observed, suggesting that the formation of pores in the current lattice struts should not be due to the collapse of keyholes as assumed in some previous work [21]. Interestingly, the highest porosity area fraction in struts, however, was found at medium laser powers (Fig. 3) and scanning speed (Fig. 4). The former may be simply because at 200 W and 225 W, the laser melt pools may have already become turbulent and the pronounced splashing may have already happened, which induced formation of considerable pores together with small struts leading to high porosity fractions. The latter is suspected to be due to unstable melt pool developed under 400 W–4000 mm/s, which is somehow implied by the development of particularly irregular-shaped struts under this condition.

The difference in the turbulence of the melt pool among different processing conditions is also suspected to be responsible for the difference in microstructure. Thus, with more violent melt pools at 400 W–7000 mm/s and 400 W–1000 mm/s than at 150 W–7000 mm/s, the convection currents in the liquid would be more turbulent, which is favourable for the creation of nucleation seeds and for the development of fine grain structure as observed in Fig. 7 [34].

Unsurprisingly, strut diameter had a significant influence on load-bearing capacity. However, strut diameter was not the only way in which processing conditions could affect load-bearing capacity; when struts become increasingly irregular in shape (for example, conditions 400 W–3000 mm/s and 400 W–4000 mm/s), the load-bearing capacity could be degraded even though their average diameter is comparable to those of more regularly-shaped struts (see Fig. 11b). Similarly, the lattice structural factor such as relative density is not the only factor that could affect compressive strengths although it did lead to continuous increase of the normalised nominal yield strength. The variation of the effective normalised nominal yield strength and effective metal strength with processing conditions suggests that other factors such as microstructure may have influenced the properties. This is

possible given that the processing condition not only affects lattice strut diameter but also the microstructure. The lowest effective normalised nominal yield strength and effective metal strength were found at 150 W–7000 mm/s (Fig. 11e), which may be due to the fact that this condition has led to the coarsest microstructure (Fig. 7a). The samples fabricated at 400 W–7000 mm/s and 400 W–1000 mm/s, however, show finer microstructure and thus higher effective normalised nominal yield strength. The dip in Fig. 11f is believed to be mainly due to the increased irregularity in strut morphology under those conditions since this has degraded the load-bearing capacity of the structures significantly as described above. The porosity level in lattice struts does not seem to affect compression properties significantly. At 150 W–7000 mm/s, the lattices showed the lowest porosity level, but this did not considerably improve their strength.

Based on the observations made on deformed samples a model for the deformation and fracture of lattice structures during compression is proposed (see Fig. 13). In stage I, the deformation of lattice structures was essentially affine (see Figs. 9b and c and 13a and b) up to the maximum stress. This was followed by shearing and breaking of the struts within a shear band at about 45° to the testing axis (for which the resolved shear stress is at a maximum), leading to a sharp drop in stress (Fig. 9a–II). Once the band has collapsed and the two neighbouring halves come in contact the stress begins to rise, the loosely attached struts in the shear band preventing the two separate lattice parts from coming into contact (Fig. 13d). With increasing stress a further shear band forms causing the stress to drop once more. This process repeats with decreasing peak stress a few times until the sample loses all integrity. Of course the sample is structurally sound only until the first compressive peak has been reached.

5. Conclusions

- (i) The diameter of the struts deviated from the design values, increasing monotonically with laser power and reaching a minimum at an intermediate scanning speed (3–4000 mm/s).
- (ii) Increased laser power led to increased molten pool width, explaining the increased strut diameter.
- (iii) During selective laser melting the melt pool underwent a repeating cycle of melt pool growth, instability followed by an abrupt shrinking causing the melt pool to become increasingly irregular-shaped and instable.
- (iv) Violent interaction between the laser beam and melt pool led to increased surface roughness and defects and is suspected to be responsible for increased internal porosity.
- (v) The load-bearing capacity of lattice structures in compression increased monotonically with strut diameter.
- (vi) Deformation of lattice structures occurred by homogeneous deformation until the maximum stress was achieved after

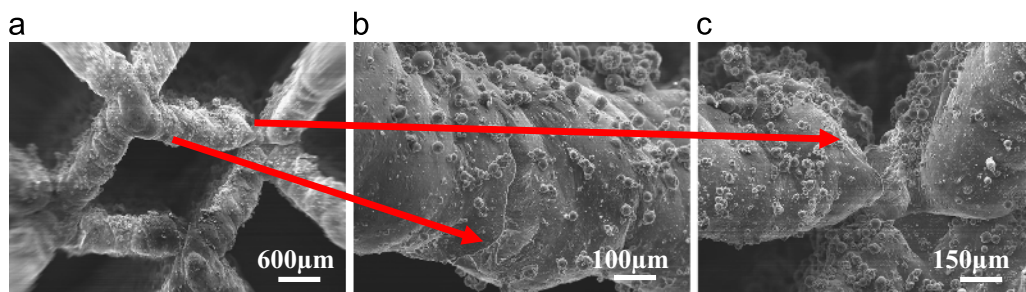


Fig. 10. Secondary electron SEM images showing the horizontal struts in a shear band in a sample tested along the Z direction.

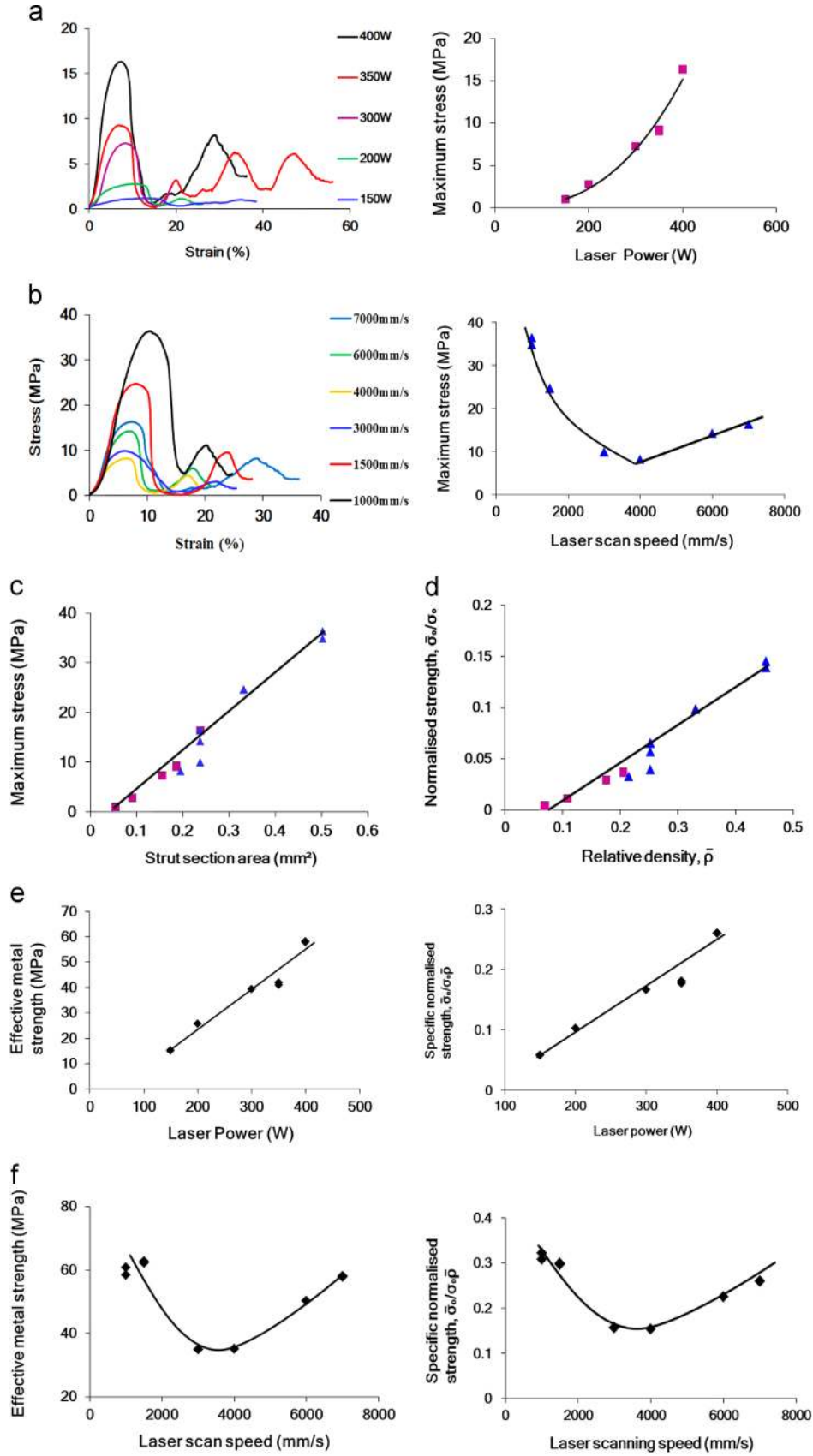


Fig. 11. Nominal engineering stress strain curves (left) and nominal (peak stresses) strengths attained (right) for lattices fabricated (a) under different laser powers at a fixed scanning speed (7000 mm/s) and (b) under different laser scanning speeds at a fixed laser power (400 W); (c) dependence of the nominal peak stress on strut diameter, (d) dependence of normalised nominal yield strength $\bar{\sigma}_o/\sigma_o$ on relative density; (e) and (f) dependence of effective metal strength (maximum load/area of struts) (left) and effective normalised nominal yield strength $\bar{\sigma}_o/\sigma_o\bar{\rho}$ (right) on laser power and scanning speed, respectively.

Table 2
Relationship between SLM processing condition and strut diameter (measured by SEM) and maximum nominal engineering strength (or nominal peak stress) of lattice structures.

Laser power–strut diameter–maximum lattice strength (at a constant scan speed of 7000 mm/s)			Laser scan speed–strut diameter–load-bearing capacity (at a constant laser power of 400 W)		
Laser power (W)	Strut diameter (μm)	Nominal peak stress (MPa)	Scan speed (mm/s)	Strut diameter (μm)	Nominal peak stress (MPa)
150	265	1.0	6000	550	14.2
200	340	1.0	4000	500	8.2
300	445	2.8	3000	550	9.9
		7.3			9.9
350	487	9.3	1500	650	24.7
		9.1			24.5
400	550	16.4	1000	800	34.8
		16.3			36.4

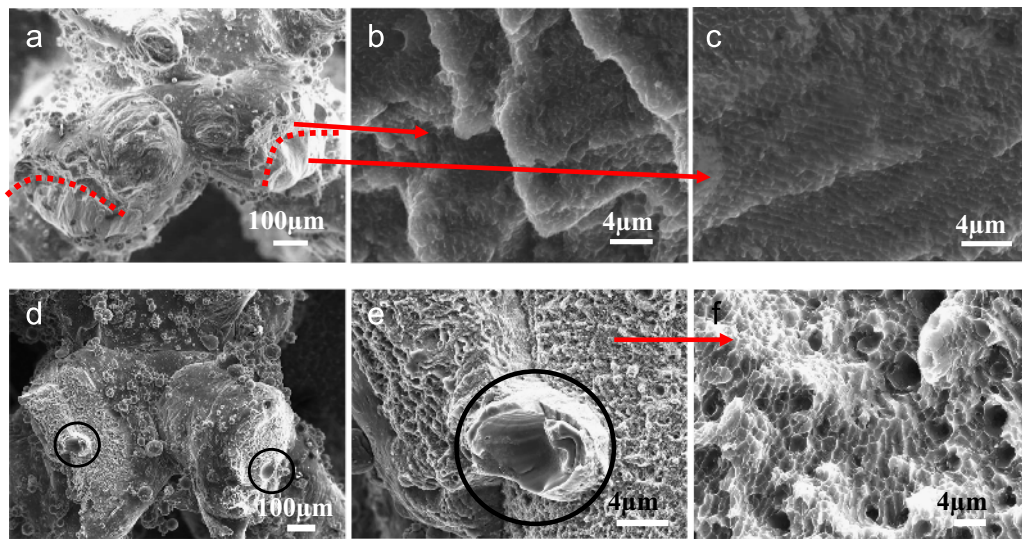


Fig. 12. Secondary electron SEM images showing typical fracture surfaces; (a–c) show the transition of fracture from ductile dimpling to lamellar fracture, the dotted lines showing the boundaries between the two stages; (d–f) fracture surface containing dimpled feature and opened-up pores. The black rings in (d) and (e) show the presence of opened-up pores.

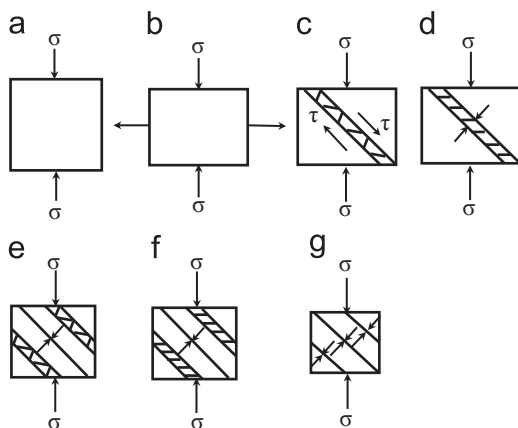


Fig. 13. Schematics showing the deformation and fracture process during compression, (a)–(b) Stage 1, deformation occurred in a homogeneous and affine manner; (c)–(d) after Stage 1, deformation occurred by developing a shear band in which the struts hinge/fracture near the nodes that connected them; (d)–(e) the loosely attached struts in the shear band disconnect leading to loss of the first shear band and bringing the split two halves into direct contact; (e)–(f), compressive force increases due to the direct contact of the two halves, leading to a new shear band; (f)–(g) struts in the new shear band disconnect, leading to lamellar fragments of lattice structures.

which the structure lost structural integrity via a series of shear banding events at around 45° to the compression axis.

Acknowledgements

The work shown in this paper is part of an AMAZE project (Additive Manufacturing Aiming towards Zero Waste and Efficient Production of High-Tech Metal Products) and was financially sponsored by the Seventh European Frame Programme (FP 7, Grant no. NMP-SE-2012-0313781). Thanks are given to Professor Michael H. Loretto for useful discussion and suggestions. (Engineering and Physical Science Research Council, UK) funding via the following Grants is also acknowledged EP/I02249X/1 and EP/F028431/1. PDL, PJW and SY are grateful to Prof Simon Phillips for accommodation and provision of facilities within the Research Complex at Harwell.

References

- [1] L.J. Gibson, M.F. Ashby, *Cellular Solids: Structure and Properties*, Cambridge University Press, Cambridge, 1997.
- [2] A.G. Evans, J.W. Hutchinsen, N.A. Fleck, M.F. Ashby, H.N.G. Wadley, *Prog. Mater. Sci.* 46 (2001) 309–327.
- [3] H. Nakajima, *Prog. Mater. Sci.* 52 (2007) 1091–1173.

- [4] T.A. Schaedler, A.J. Jacobsen, A. Torrents, A.E. Sorensen, J. Lian, J.R. Greer, L. Valdevit, W.B. Carter, *Science* 334 (2011) 962–965.
- [5] P. Heintl, L. Muller, C. Körner, R.F. Singer, F.A. Muller, *Acta Biomater.* 4 (2008) 1536–1544.
- [6] L. Mullen, R.C. Stamp, W.K. Brooks, E. Jones, C.J. Sutcliffe, J. Biomed. Mater. Res. Part B: Appl. Biomater. 89B (2009) 325–334.
- [7] M.A. Lopez-Heredia, E. Goyenvalle, E. Aguado, P. Pilet, C. Leroux, M. Dorget, P. Weiss, P. Layrolle, J. Biomed., *Mater. Res. A* 85 (2008) 664–673.
- [8] C.Z. Yan, L. Hao, A. Hussein, S.L. Bubb, P. Young, D. Raymont, J. Mater. Process. Technol. 214 (2014) 856–864.
- [9] C.Z. Yan, L. Hao, A. Hussein, D. Raymont, *Int. J. Mach. Tools Manuf.* 62 (2012) 32–38.
- [10] C.Z. Yan, L. Hao, A. Hussein, P. Young, D. Raymont, *Mater. Des.* 55 (2014) 533–541.
- [11] R. Gümrük, R.A.W. Mines, S. Karadeniz, *Mater. Sci. Eng. A* 586 (2013) 392–406.
- [12] R. Gümrük, R.A.W. Mines, *Int. J. Mech. Sci.* 68 (2013) 125–139.
- [13] S. McKown, Y. Shen, W.K. Brookes, C.J. Sutcliffe, W.J. Cantwell, G.S. Langdon, G. N. Nurick, M.D. Theobald, *Int. J. Impact Eng.* 35 (2008) 795–810.
- [14] B. Gorny, T. Niendorf, J. Lackmann, M. Thoene, T. Troester, H.J. Maier, *Mater. Sci. Eng. A* 528 (2011) 7962–7967.
- [15] M. Smith, Z. Guan, W.J. Cantwell, *Int. J. Mech. Sci.* 67 (2013) 28–41.
- [16] S. Babaei, B.H. Jahromi, A. Ajdari, H. Nayeib-Hashemi, A. Vaziri, *Acta Mater.* 60 (2012) 2873–2885.
- [17] G. Campoli, M.S. Borleffs, S.A. Yavari, R. Wauthle, H. Weinans, A.A. Zadpoor, *Mater. Des.* 49 (2013) 957–965.
- [18] K. Kempen, L. Thijs, E. Yasa, M. Badrossamay, W. Verheecke, J.-P. Kruth, Process optimization and microstructural analysis for selective laser melting of AlSi10Mg, in: Proceedings of Annual International Solid Freeform Fabrication Symposium – An Additive Manufacturing Conference, The University of Texas at Austin, USA, 2011.
- [19] P.A. Kobryn, S.L. Semiatin, Mechanical properties of laser-deposited Ti–6Al–4V, in: Solid Freeform Fabrication Symposium Proceedings, Austin, 2001.
- [20] S. Das, *Adv. Eng. Mater.* 5 (2003) 701–711.
- [21] L. Thijs, K. Kempen, J.-P. Kruth, J.V. Humbeeck, *Acta Mater.* 61 (2013) 1809–1819.
- [22] L. Thijs, L. Verhaeghe, T. Craeghs, J.V. Humbeeck, J.-P. Kruth, *Acta Mater.* 58 (2010) 3303–3312.
- [23] T. Vilaro, C. Colin, J.D. Bartout, *Metall. Mater. Trans. A* 42 (2011) 3190–3199.
- [24] C.L. Qiu, N.J.E. Adkins, M.M. Attallah, *Mater. Sci. Eng. A* 578 (2013) 230–239.
- [25] S. Yue, P.D. Lee, G. Poolagasundarampillai, J.R. Jones, *Acta Biomater.* 7 (2011) 2637–2643.
- [26] T.B. Kim, S. Yue, Z.Y. Zhang, E. Jones, J.R. Jones, P.D. Lee, J. Mater. Process. Technol. 214 (2014) 2706–2715.
- [27] C.I. Hammetter, R.G. Rinaldi, F.W. Zok, J. Appl. Mech. 80 (2013) (041015-1 ~ 11).
- [28] C.I. Hammetter, F.W. Zok, J. Appl. Mech. 81 (2014) (011006-1 ~ 11).
- [29] G.W. Kooistra, V.S. Deshpande, H.N.G. Wadley, *Acta Mater.* 52 (2004) 4229–4237.
- [30] D.S. Nagesh, G.L. Datta, J. Mater. Process. Technol. 123 (2002) 303–312.
- [31] M. Shueb, M. Parvez, P. Kumari, *Int. J. Eng. Sci. Technol.* 5 (2013) 200–212.
- [32] A.P. Tadamalle, Y.P. Reddy, E. Ramjee, *Adv. Prod. Eng. Manag.* 8 (2013) 52–60.
- [33] A. Aloraier, A. Almazrouee, T. Shehata, J.W.H. Price, J. Mater. Eng. Perform. 12 (2012) 540–547.
- [34] P.A. Porter, K.E. Easterling, *Phase Transformations in Metals and Alloys*, second ed., Chapman & Hall, London (1992) 236.